nature physics

Article

https://doi.org/10.1038/s41567-024-02651-5

# Self-propulsion, flocking and chiral active phases from particles spinning at intermediate Reynolds numbers

Received: 11 March 2024

Accepted: 26 August 2024

Published online: 08 October 2024

Check for updates

Panyu Chen[1,6], Scott Weady[2,6], Severine Atis[1,5,6], Takumi Matsuzawa[1], Michael J. Shelley[2,3] & William T. M. Irvine[1,4]

Vorticity, a measure of the local rate of rotation of a fluid element, is the driver of incompressible flow. In viscous fluids, powering bulk flows requires the continuous injection of vorticity from boundaries to counteract the diffusive effects of viscosity. Here we power a flow from within by suspending approximately cylindrical particles and magnetically driving them to rotate at Reynolds numbers in the intermediate range. We find that a single particle generates a localized three-dimensional region of vorticity around it—which we call a vortlet—that drives a number of remarkable behaviours. Slight asymmetries in the particle shape can deform the vortlet and cause the particle to self-propel. Interactions between vortlets are similarly rich, generating bound dynamical states. When a large number of vortlets interact, they spontaneously form collectively moving flocks. These flocks remain coherent while propelling, splitting and merging. If enough particles are added so as to saturate the flow chamber, a homogeneous three-dimensional active chiral fluid of vortlets is formed, which can be manipulated with gravity or flow chamber boundaries, leading to lively collective dynamics. Our findings demonstrate an inertial regime for synthetic active matter, provide a controlled physical system for the quantitative study of three-dimensional flocking in non-sentient systems and establish a platform for the study of three-dimensional active chiral fluids.

Pushing on a body of water produces a myriad of mesmerizing flow structures. A vortex ring is a classic example: impulsively forcing water through an orifice generates a ring of concentrated vorticity that advects itself over long distances, carrying the inertia of the initial impulse[1,2]. This capacity for self-sustained liveliness of a flow is lost when viscosity, rather than inertia, dominates. Indeed, the fluid inside microscopic living cells shows little tendency to flow unless continuously forced by active elements[3,4]. These differences are reflected in the equations of fluid motion; viscous Stokes flows are linear, famously time reversible, with the space of responses to actuation strongly limited compared with that of nonlinear and often unruly near-inviscid flows[5,6].

A realm of possibilities lies in the middle where viscosity and inertia compete[7–9]. Here, the symmetries of Stokes flow are broken by inertia, lifting substantial constraints on the flow, while viscous effects promote dynamical regularity. The result is a rich space of allowed dynamics involving spontaneous locomotion[10–12] and hydrodynamic synchronization[13–15]. Because of the presence of viscous dissipation,

[1]James Franck Institute and Department of Physics, University of Chicago, Chicago, IL, USA. [2]Center for Computational Biology, Flatiron Institute, New York, NY, USA. [3]Courant Institute, New York University, New York, NY, USA. [4]Enrico Fermi Institute, University of Chicago, Chicago, IL, USA. [5]Present address: Institut Pprime, CNRS, Université de Poitiers, Institut supérieur de l'aéronautique et de l'espace-École nationale supérieure de mécanique et d'aérotechnique, Poitiers, France. [6]These authors contributed equally: Panyu Chen, Scott Weady, Severine Atis. e-mail: mshelley@flatironinstitute.org; wtmirvine@uchicago.edu

https://doi.org/10.1038/s41567-024-02651-5

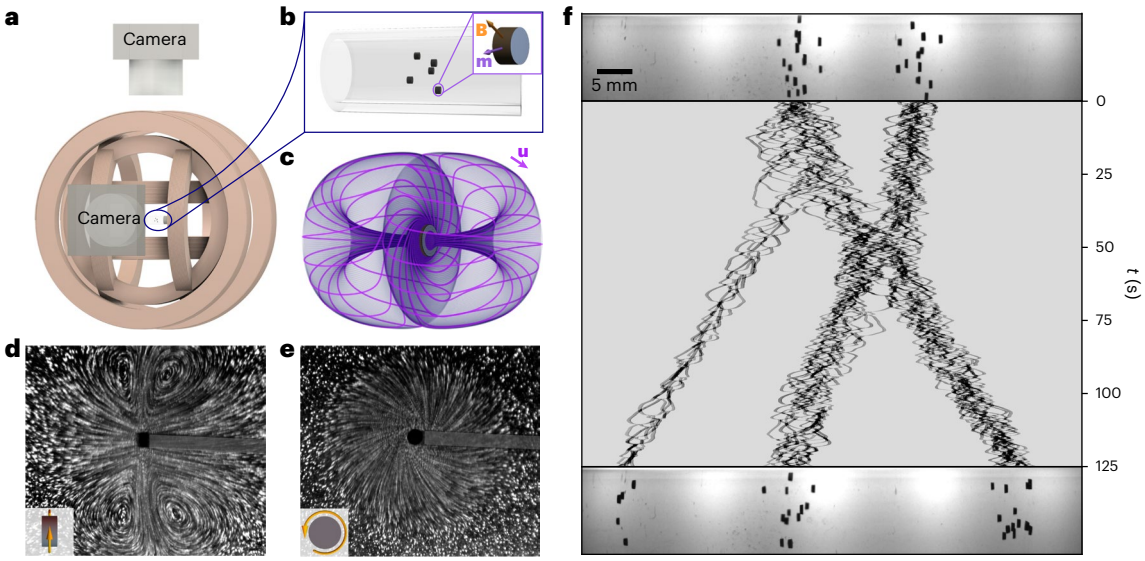


**Fig. 1 | Suspensions of spinning particles and their vortlets self-organize into flocks. a**, Our experiment utilizes suspended, magnetically polarized PDMS cylindrical particles with a permanent dipole moment **m**, which are forced to rotate about their symmetry axis under a rotating magnetic field **B**. This generates a three-dimensional 'vortlet' flow, distinct from that of the rotlet of Stokes flow. **b**, The particles are suspended within a vial in a density-matched $Na_2WO_4$–water solution. **c**, Numerical computation of the flow field around a single particle at $Re_\Omega = 30$, visualized through streamlines, shows the characteristic bound vortlet flow, which consists of a large rotational component accompanied by inflow along the axis of rotation and outflow along the sides. **d**,**e**, The vortlet flow field is visualized using time-lapsed images of tracer particles in the plane perpendicular to the plane of rotation (**d**) and in the plane of rotation (**e**). The grey area on the right of the particle corresponds to its shadow. **f**, By removing the background and integrating the image intensity across the flow chamber, we generate vertically averaged kymographs that capture the three-dimensional collective dynamics of 30 vortlets as vortlet flocks propagate, merge, exchange and split. Panel **f** corresponds to Supplementary Movie 1.

just like their counterparts at low Reynolds number[16–21], these flows require continuous activation.

Vorticity, which is naturally created by fluid flowing past walls, plays a unique role in incompressible flow, acting as a source of its dynamics. When generated through internal boundaries in viscous flows, for example, by rotating microscopic particles, dynamical states emerge that include collective motion[22–24], hydrodynamic crystallization[25–28], macroscopic chiral stresses[29–36] and non-reciprocity[37–39]. Much less is known, however, about these flows at non-zero Reynolds numbers where the fluid itself carries advective nonlinearities. In this case, the inertia of the background fluid can break fundamental assumptions such as pairwise additivity of forces between particulates and can substantially modify the bulk rheology of a suspension[40].

We set out to leverage vorticity as a source of dynamics in inertial flow by driving suspended particles to rotate at intermediate Reynolds numbers. Our experimental platform, illustrated in Fig. 1a,b, consists of a collection of approximately cylindrical particles, produced by laser-cutting disks of diameter ~1 mm from a ~0.6-mm-thick film of magnetically doped polydimethylsiloxane (PDMS)[41]. The particles are magnetized by passage between a pair of rare-earth magnets, endowing them with a permanent magnetic dipole moment **m** perpendicular to their axis of symmetry as shown in Fig. 1b.

The particles are suspended in a density-matched $Na_2WO_4$–water solution and placed in a flow chamber that in turn is placed in a set of three mutually orthogonal Helmholtz coil pairs. The coils are programmed to produce a steerable magnetic field rotating in planes orthogonal to an axis $\hat{\mathbf{\Omega}}$. The particles experience a torque and spin about $\hat{\mathbf{\Omega}}$ at the drive frequency $f$, up to a frequency beyond which the maximum magnetic torque is insufficient to balance the viscous response torque (Supplementary Information). With this method of actuation, we access rotational Reynolds number $Re_\Omega = \Omega R^2/\nu \approx 5-200$, where $\Omega = 2\pi f$, $\nu$ is the kinematic viscosity and $R$ is the radius of the cylindrical spinner.

Each spinner creates a localized flow, whose streamlines are represented in Fig. 1d, consisting of a predominantly rotational flow about the axis of rotation, together with inflows along the axis of rotation, similar to the secondary flow induced by a rotating sphere[42,43]. These inflows are accompanied by aligned, oppositely rotating vortex rings that sit above and below the spinner as shown in Fig. 1d,e (see Supplementary Information for details). This 'vortlet' structure differs fundamentally from a Stokesian rotlet whose flow is only rotational with no intrinsic lengthscale. Like the rotlet, the vortlet requires continuous actuation to be sustained, but unlike the rotlet, it has a non-zero relaxation time. We will refer to this flow–particle pair interchangeably as spinner, to focus on the particle, or vortlet to emphasize the bound flow.

Remarkably, when many suspended spinners are simultaneously driven to rotate about an axis parallel to the cylindrical flow chamber, they self-organize into cohesive groups that propagate along the flow chamber, their dynamics punctuated by isolated splitting and merging events, reminiscent of those seen in natural flocks. The vertically averaged kymograph in Fig. 1f, constructed by averaging the image intensity orthogonal to the plane of spin (the vertical direction in the image), provides an illustrative visualization. Initially, the spinners form two coherent flocks that propagate towards one another. After a short time (which increases downwards in the kymograph), a smaller flock separates from the flock on the left, after which the two larger flocks merge. After ~10 s, this merged flock splits in turn. Following each merging or splitting event, the flocks change speed as seen in the slope of the trajectory on the kymograph. These striking collective dynamics raise fundamental questions: What determines a flock's speed? What determines whether a flock stays together?

To gain insight into how these complex collective dynamics emerge, we first examine the dynamics of single spinners driven to rotate in isolation within a tube of 12.7 mm diameter. Figure 2a(left) shows a typical vertically averaged kymograph. While in some cases the spinner simply rotates in place, in most cases, such as this one, it

https://doi.org/10.1038/s41567-024-02651-5

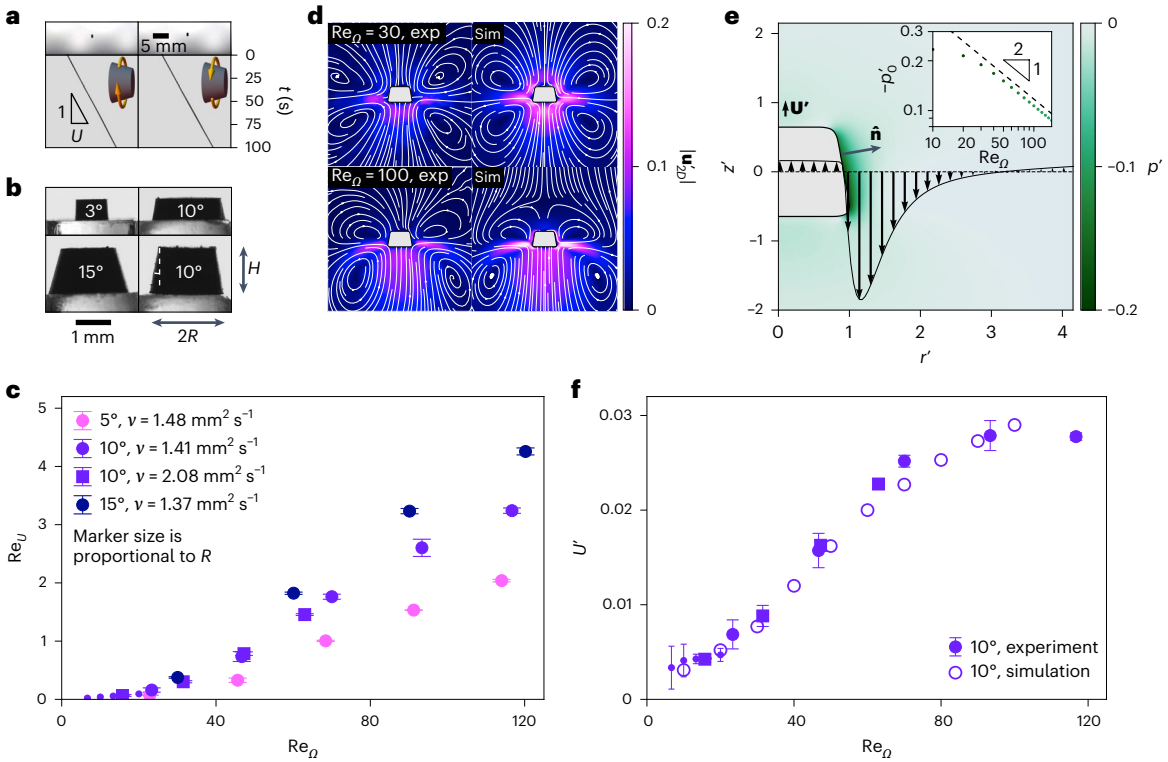


**Fig. 2 | A spinner's shape harvests the active pressure to drive self-propulsion.** **a**, Vertically averaged kymographs of the same single spinner show self-propulsion under clockwise and counterclockwise rotation, with no evident change in either speed or direction. **b**, A collection of moulded particles of varying size, side angle and aspect ratio. **c**, The propulsive Reynolds number $\mathrm{Re}_U = UR/\nu$ of spinners as a function of their driving rotational Reynolds number $\mathrm{Re}_\Omega = \Omega R^2/\nu$ for spinners of different sizes $R$ and $H$ and side angles $\beta$, in carrier fluids of different viscosities $\nu$. The size of each marker is proportional to the radius $R$ of the spinner (~0.2 mm; ~1 mm). Within our experimental range, $\mathrm{Re}_U$ increases monotonically as a function of $\mathrm{Re}_\Omega$. **d**, Experimental PIV (exp, left column) of a spinner particle with $R = 1.02$ mm, $\alpha = 1.24$, $\beta = 10^\circ$ at $\mathrm{Re}_\Omega = 30$ (top row) and $\mathrm{Re}_\Omega = 100$ (bottom row) compared with the simulation (sim, right column). **e**, From simulation, a zoomed-in view of the boundary layer of the spinner, showing the local fluid dimensionless pressure field $p' = p/\rho\Omega^2R^2$ and vertical velocity profile. The inset displays the relationship between the dimensionless wall pressure $p'_0$ at the mid-plane of the particle and $\mathrm{Re}_\Omega$ in simulation, in agreement with the boundary layer theory prediction of a $\mathrm{Re}^{-1/2}$ power law. **f**, Dimensionless speed $U' = \mathrm{Re}_U/\mathrm{Re}_\Omega$ versus $\mathrm{Re}_\Omega$ for spinners of different radii but with same angle $\beta = 10^\circ$ and similar aspect ratios in fluids of different viscosities, compared with simulations of a spinner with the same angle and aspect ratio. The error bar represents one standard deviation of speeds extracted from four independent trajectories. Panel **a** corresponds to Supplementary Movie 2.

propels at a constant velocity along its axis of rotation, with a speed $U$ that changes with the rotation rate $\Omega$. In addition, when the rotation of the magnetic field is reversed, the direction and magnitude at which the spinner propels is unaffected, as shown in Fig. 2a(right). This is in striking contrast to Stokesian dynamics where time reversibility would imply a reversal of $U$ in response to the reversal of the driving rotation $\Omega$. Hence, the origin of propulsion must be inertial.

Under symmetry considerations, we would not expect a rotating cylinder to propel, which leads to the question of how symmetry is broken. High-magnification images of our particles, examples of which are shown in Supplementary Fig. 2, reveal that many of the particles are in fact not perfect cylinders. Their geometries present varying degrees of asymmetry but are generally reminiscent of a truncated cone or a conical frustum. These shapes are axisymmetric and therefore lack chirality, but break head-tail symmetry. We find that rotating particles of this form propel in the direction of the narrower end.

As in all cases of propulsion at finite Reynolds number, the propulsive Reynolds number $\mathrm{Re}_U = UR/\nu$, which characterizes the speed of propulsion $U$, is a function of the 'active' Reynolds number $\mathrm{Re}_\Omega$ and of the particle geometry. To quantify this relationship, we constructed moulds to produce particles in the shape of a conical frustum, controlling the bottom radius $R$, aspect ratio $\alpha = H/R$ and side angle $\beta$, which we characterized using a custom imaging setup (Supplementary Information). Figure 2b displays a selection from our spinner collection.

Figure 2c shows the propulsive Reynolds number $\mathrm{Re}_U$ as a function of $\mathrm{Re}_\Omega$ for several values of $\beta$. For the particles presented here, we find that self-propulsion is insensitive to $\alpha$ as shown in Supplementary Fig. 23. The propulsive Reynolds number $\mathrm{Re}_U$ increases monotonically in the range $\beta = 0$–$15^\circ$.

Curiously, the dimensionless velocity $U' = \mathrm{Re}_U/\mathrm{Re}_\Omega = U/R\Omega$, shown in Fig. 2f, indicates two regimes of self-propulsion: for low rotational Reynolds numbers, $U'$ strongly depends on $\mathrm{Re}_\Omega$, but is approximately constant for $\mathrm{Re}_\Omega$ values larger than ~80. This suggests the drag becomes nonlinear in the velocity, which may be due to a combination of both inertial effects and drag enhancement by rotation, which occurs even at low Reynolds numbers[44,45].

To investigate the mechanics of propulsion, we performed simulations of the Navier–Stokes equations coupled to the free motion of a frustum-shaped body rotating under an external torque (Supplementary Information). The numerical method uses a volume-penalization scheme to account for fluid–structure interactions[46,47]. Figure 2d shows simulated velocity fields around a single spinner, for $\mathrm{Re}_\Omega = 30$ and $\mathrm{Re}_\Omega = 100$, next to the corresponding experimental flow fields determined by particle imaging velocimetry (PIV). As $\mathrm{Re}_\Omega$ increases from 30 to 100, the oppositely oriented vortex rings identified in Fig. 1d become increasingly distorted and swept back towards the wider end of the particle, gradually giving rise to a circular jet.

Closer inspection of the simulated flow, in particular the pressure distribution, reveals a novel underlying propulsive mechanism.

https://doi.org/10.1038/s41567-024-02651-5

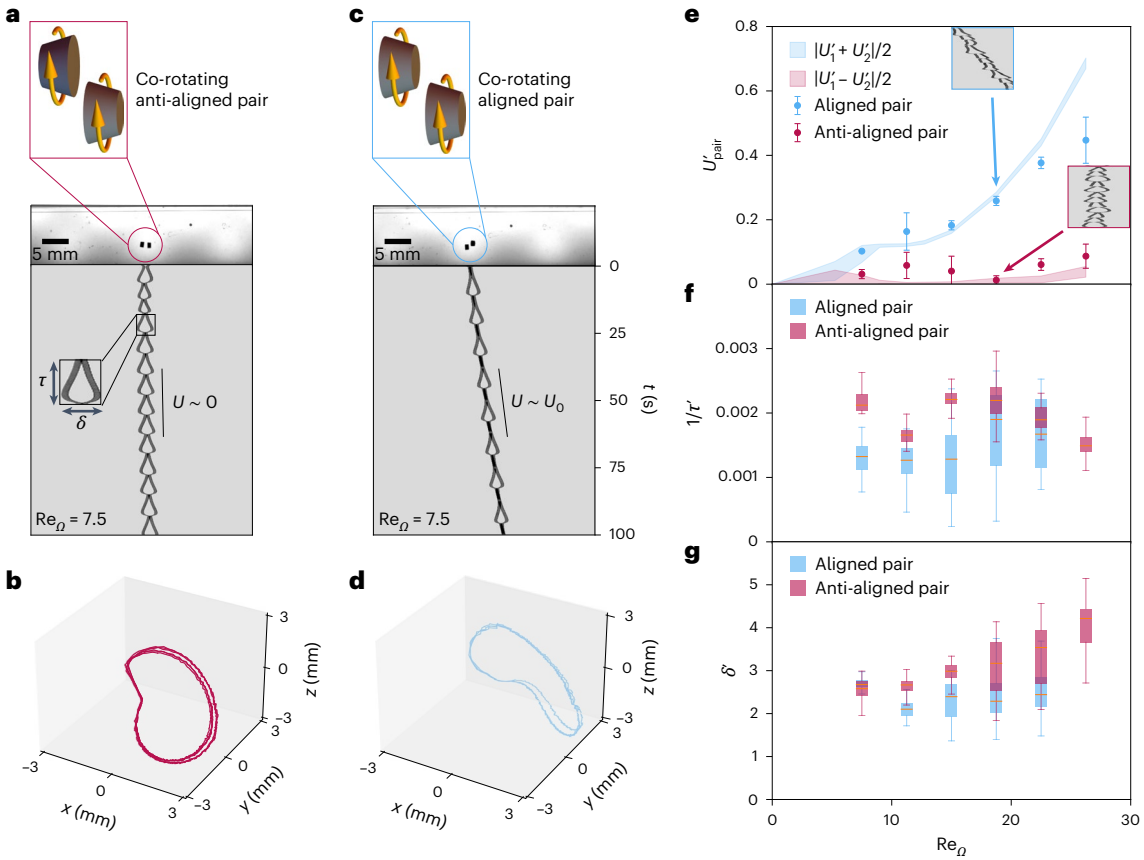


**Fig. 3 | Two spinners orbit while self-propelling, with their dynamics dictated by their configuration. a**,**c**, Configuration diagrams, experimental snapshots and vertically averaged kymographs of an anti-aligned (**a**) and an aligned (**c**) pair. From the kymograph we can extract the pair speed $U$, orbital period $\tau$ and orbital width $\delta$. **b**,**d**, The relative three-dimensional trajectory of the anti-aligned (**b**) and the aligned (**d**) pairs in **a** and **c**. **e**, Dimensionless self-propulsion of the pair $U' = U/\Omega R$ versus rotational Reynolds number $\mathrm{Re}_\Omega$ of a single spinner, compared with prediction from single particle speeds $U_1$ and $U_2$. The error bar represents one standard deviation of four independent measurements. **f**,**g**, The dimensionless orbital frequency $1/\tau' = 1/\Omega\tau$ (**f**) and dimensionless orbital width $\delta' = \delta/R$ (**g**) versus rotational Reynolds number $\mathrm{Re}_\Omega$. Each data point is derived by combining cycles from four independent trajectories, totalling approximately 100 cycles. The box shows data in the interquartile range, and the line indicates the median. The whiskers extend to the farthest data points within 1.5 times the interquartile range from the box. Panels **a** and **c** correspond to Supplementary Movie 3.

Figure 2e shows the pressure field $p$ around the spinner, and the vertical velocity field at its mid-plane $z = 0$. Both show a boundary layer structure, with a sharp low-pressure region cladding the spinner sides. This active pressure bubble arises from the rotational drive, and its sign is independent of the direction of rotation. The nature of propulsion can then be discerned by considering the pressure force acting on the spinner, given by $\mathbf{F}_\mathrm{p} = \int_S (-p\hat{\mathbf{n}})\,\mathrm{d}S$, where $S$ is the spinner surface and $\hat{\mathbf{n}}$ is its outward normal. From Fig. 2e we see that the pressure on the spinner top and bottom is close to the zero far-field pressure, making little contribution to the pressure force. The side walls tell a different story. If the side walls are straight, that is, $\beta = 0°$, then the up–down symmetry of $p$ yields $\mathbf{F}_\mathrm{p} = 0$ and a zero mid-plane vertical velocity. But, for this frustrum shape, the side wall tilt gives $\hat{\mathbf{n}}$ an upwards component so that $\hat{\mathbf{n}} \cdot \hat{\mathbf{z}} > 0$ within the bubble of negative pressure. Consequently $\hat{\mathbf{z}} \cdot \mathbf{F}_\mathrm{p} > 0$, which drives the spinner upwards, towards its narrower end. In essence, tilt allows the spinner to harvest some of the energy stored in its active pressure bubble, with its speed $U$ arising from the active pressure force being balanced by the viscous fluid drag on spinner motion. The velocity boundary layer also arises from the active force, where fluid is pushed downwards as the body moves upwards, thus exchanging momentum between the body and the fluid.

While the active pressure drop is reminiscent of the pressure lows realized within intense fluid vortices that scale with $\Omega^2$, for $\mathrm{Re}_\Omega \gtrsim 40$ we find the relationship between the pressure drop and rotation, as computed numerically on a stationary particle, scales as $p \sim \Omega^{3/2}$ (Fig. 2e, inset). This scaling is a hallmark of boundary layers on rotating bodies at high Reynolds numbers[45,48]. The transition to this scaling is accompanied by the formation of localized jets that can be seen in Fig. 2d.

Having investigated the dynamics of a single spinner, we next consider interactions between pairs of spinners in the same tube. At sufficiently low rotational drive, the hydrodynamic forces are weak by comparison with magnetic interactions (Supplementary Information). In this regime, magnetic particles rotating at low Reynolds numbers are known to cluster in planes under the influence of their time-averaged magnetic interactions[49,50]. We find that, at higher drives, where magnetic interactions are weak compared with hydrodynamic forces, adding a second spinner with a closely matched geometry and density to the chamber generally results in dynamics of the type shown in Fig. 3. In particular, we observe bound quasi-periodic three-dimensional orbits. As seen in the vertically averaged kymograph of Fig. 3a, though the two spinners have opposing propulsive directions, they remain bound to each other with their joint centre of mass nearly stationary. In contrast, when the two bound spinners move in the same direction, as shown in Fig. 3c, they travel together at the speed of a single spinner while orbiting each other with a slightly longer period compared with that of their anti-aligned counterpart. The relative three-dimensional trajectory of the pairs in Fig. 3a,c are shown in Fig. 3b,d, respectively. These show the orbits are closed in three dimensions and not only in their projections.

To gain insight into these pair interactions, we perform numerical simulations of idealized configurations consisting of two spinners

https://doi.org/10.1038/s41567-024-02651-5

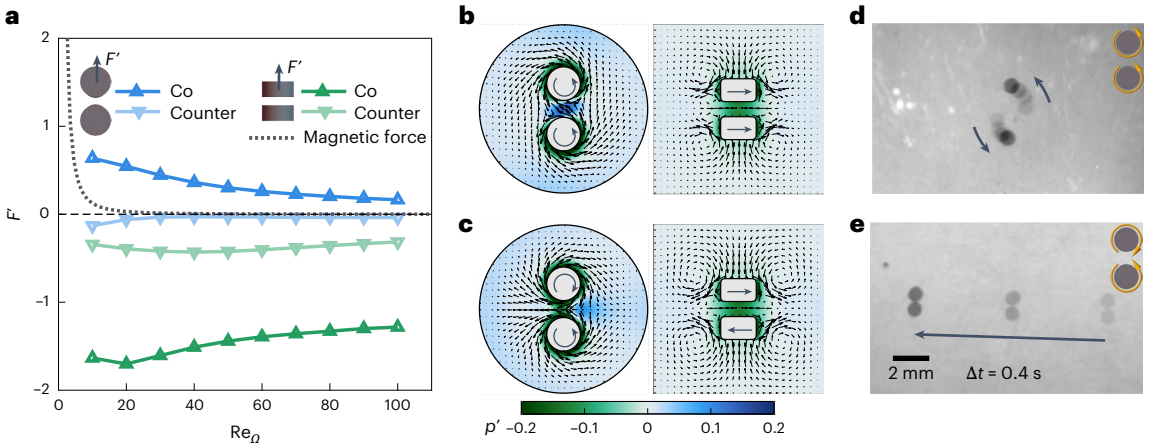


**Fig. 4 | Binding and propulsion mechanics of pairs of co- and counter-rotating spinners. a**, Hydrodynamic forces between co-rotating and counter-rotating pairs from simulation. The direction of the measured force is indicated in the legend. Both pairs attract when stacked vertically. A co-rotating pair repels in the rotation plane, while a counter-rotating pair, generated by driving the spinners with a uniaxial oscillating magnetic field, attracts in the rotation plane. The magnitude of magnetic interactions is also shown, which has a substantially lower magnitude than the hydrodynamic force. **b**,**c**, Simulated flow field and pressure fields around co-rotating (**b**) and counter-rotating (**c**) pairs. **d**,**e**, A time-lapsed image of experiments of co-rotating (**d**) and counter-rotating (**e**) pairs. Transparency indicates time. Panels **d** and **e** correspond to Supplementary Movie 4.

held in place and separated by one particle radius. A calculation of the hydrodynamic force between the co-rotating spinners (Fig. 4a–c) reveals that they are attractive when vertically aligned and repulsive when horizontally aligned. These signed interactions are manifest in the experiment shown in Fig. 4d in which two co-rotating spinners were activated in the centre of a large container. The spinners attract vertically and then spiral away from each other radially. Interestingly, we find that if one of the spinners is rotated in the opposite direction, the two bind in the radial direction and propel as a pair (Fig. 4e). This is reflected in the numerical calculation that shows that counter-spinners are attractive in both the radial and vertical directions. We note that these dynamics are forbidden at low Reynolds numbers, since time reversal symmetry of the Stokes equations guarantees that the spinners must remain at a constant distance; otherwise, any motion towards each other would have to be reversed when the spin is reversed.

The central role of self-propulsion in determining the pair dynamics is made clear by quantifying the relationship between individual spinner speeds and the bound pair speed and orbital period. We measure the speed of the pair of spinners by linearly fitting the mean of the kymograph, and measure the extent of the pair by averaging twice the standard deviation of the kymograph over time. Interestingly, the average of the independently measured speeds $U_1$ and $U_2$ provides an excellent predictor of the speed of the bound pair. This is shown in Fig. 3e, where we see that the anti-aligned pair moves approximately at a speed of $|U_1 - U_2|/2$ while an aligned pair moves at a speed of $|U_1 + U_2|/2$. Similarly, we find the orbital period $\tau' = \Omega\tau$ is shorter for anti-aligned spinners than for aligned spinners when the pair is regular ($\mathrm{Re}_\Omega \leq 15$) (Fig. 3f), while the average distance between them $\delta' = \delta/R$ is comparable (Fig. 3g). See Supplementary Section Vc for further discussion of the effect of vial diameter on pair dynamics. As the Reynolds number is increased, the orbits no longer appear to be periodic, though they remain bounded, and the pair's speed is less than the average of the individual signed speeds.

As more spinners are added to the flow chamber, these elegant dynamics rapidly lose coherence and transition to the chaotic collective dynamics visible in Fig. 5. Despite the loss of coherence, the spinners nonetheless bind and exhibit flocking behaviour. It is natural to ask to what extent the collective dynamics inherit that of single spinners. For a pair of spinners, we found that the relative orientation of individual spinners was predictive of the pair's velocity and controls the orbital period. A naive generalization of the pair dynamics would suggest that the velocity of a flock is given by the average velocity of the individuals, $U_{\mathrm{flock}} = (1/N)\sum_{i=1}^{N} U_i$, where $U_1, U_2, \ldots, U_N$ are the signed speeds of the individual spinners. For flocks of spinners of similar speeds $|U_i| \approx U_0$, we then have

$$U_{\mathrm{flock}} \approx \left(\frac{N_\mathrm{r} - N_\mathrm{l}}{N_\mathrm{r} + N_\mathrm{l}}\right) U_0, \tag{1}$$

where $N_\mathrm{r}$ and $N_\mathrm{l}$ denote the number of particles oriented to the right and left, respectively. The coefficient $(N_\mathrm{r} - N_\mathrm{l})/(N_\mathrm{r} + N_\mathrm{l})$ is the polarization of the flock, which takes values ±1 when all particles point in the same direction and 0 when an equal number point in either direction.

We assess this prediction by visually determining the polarization of flocks of $N = 2$, 3 and 20 spinners at rotational Reynolds numbers $\mathrm{Re}_\Omega = 5$–20. Furthermore, we simulated flocks of $N = 5$ spinners in the same range of $\mathrm{Re}_\Omega$. Figure 5c shows the resulting aggregate plot of the flock speed against the polarization, revealing a linear relation in agreement with equation (1). Thus, even within the chaos of a flock, individual propulsion plays a key role in determining the dynamics of the whole.

This relationship between flock speed and polarization lends a natural interpretation to the changes of speed observed in Fig. 1f. As the flocks merge and split, their polarization and, thus, their collective speed change accordingly. During this process, visual inspection shows that changes of particle orientation are rare (Supplementary Information). Given a collection of flocks $m = 1, \ldots, M$, each with $N_m$ particles and mean velocity $U_{\mathrm{flock},m}$, we define $P_m = N_m U_{\mathrm{flock},m}/U_0$ as the 'thrust' of the flock. Merging or splitting events then obey

$$\sum_{m=1}^{M^-} P_m^- = \sum_{m=1}^{M^+} P_m^+, \tag{2}$$

where minus and plus superscripts denote before and after the event, respectively. Examples of both splitting and merging events of two flocks are shown in Fig. 5a,b. From a collection of such events, we extracted the before and after thrusts and compared them in Fig. 5d. The linear relation with unit slope confirms the empirical validity of equation (2).

A defining feature of a flock is its ability to stay cohesive. Strikingly, as shown in Fig. 5e, the lifetime of our flocks increases with the number of particles and can exceed several minutes. For example, at 25 Hz ($\mathrm{Re}_\Omega \approx 20$), a flock of 50 particles typically splits within 100 s,

https://doi.org/10.1038/s41567-024-02651-5

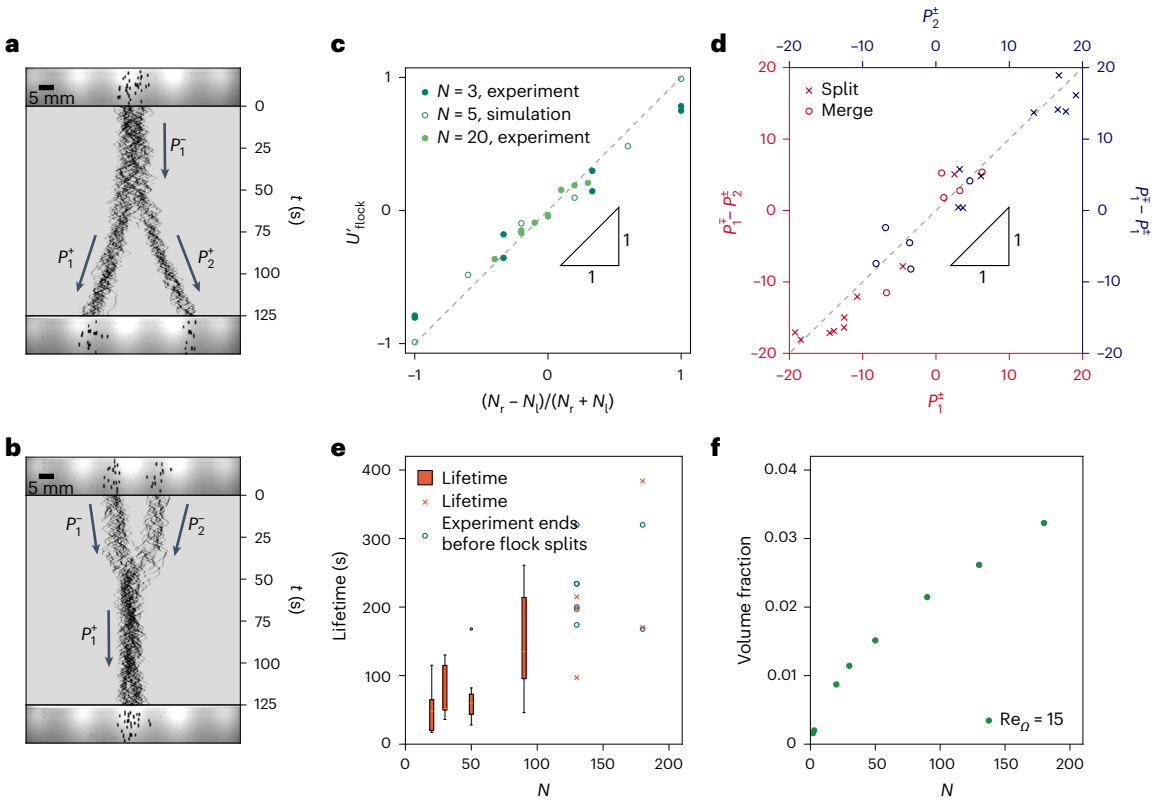


**Fig. 5 | Flock speed depends on its polarization; total thrust is conserved during merges and splits; lifetime and volume fraction vary with particle number. a**,**b**, Vertically averaged kymographs showing splitting (**a**) and merging (**b**) events. Each flock is assigned a dimensionless thrust $P_m = N_m U_{flock,m}/U_0$, where $N_m$ is the number of particles in the flock, $U_{flock,m}$ is the flock speed and $U_0$ is the average speed of the particles. **c**, The dimensionless flock speed $U'_{flock} = U_{flock}/U_0$ is determined by the polarization of the flock $(N_r - N_l)/(N_r + N_l)$. **d**, When flocks merge or split, their total thrust stays constant. **e**, At 25 Hz ($Re_\Omega = 20$), the flock lifetime increases with the number of particles in the flock. The flock's lifetime is measured when 20% of the particles separate from the flock. The box shows data in the interquartile range, and the line indicates the median. The whiskers extend to the farthest data points within 1.5 times the interquartile range from the box. The data points outside the whiskers are shown as the fliers. The box plot contains five or more independent measurements. **f**, The volume fraction of a flock increases with its particle number at $Re_\Omega = 15$. Panels **a** and **b** correspond to Supplementary Movie 5.

but a flock with more than 150 particles persists for more than 200 s. Moreover, the flock density also increases with the number of particles as shown in Fig. 5f, a behaviour analogous to the increasing density of a school of fish with the number of its constituents[51]. This remarkable tendency to become more cohesive the more members are added to the flock is contrasted by a tendency to become less cohesive when the rotational drive is increased and mixed-polarization flocks split into purely polarized ones.

The formation of flocks in our tubular chambers arises from the interplay of spinner–spinner interactions, confinement and self-propulsion. Confinement keeps the spinners from drifting apart sideways and makes them re-circulate, which in turn lines them up along the tube's axis. Axially aligned spinners then attract as shown in Supplementary Fig. 26. This attraction decays as the particles move off axis, even becoming repulsion when sufficiently askew, creating the possibility for configurations in which self-propulsion beats attraction. How to generalize these pairwise interactions to the flock splitting phenomenon remains an open question not least because of the inherent non-additivity of pairwise forces at finite Reynolds numbers. Indeed, experiments often show flocks splitting into two subflocks each with dozens of particles, suggesting further that flock splitting must be collective in nature.

As more spinners are added, the flock size grows until it becomes comparable to the length of the flow chamber, at which point the spinners are attracted to and gradually absorbed by the end caps, an effect that is known to occur for particles rotating near a flat wall at non-zero Reynolds numbers[52]. This raises the question of whether, if at all, the chaotic three-dimensional dynamics of a collection of spinners and their vortlets can generalize to a steady-state phase of uniform density spanning the flow chamber.

Figure 6a,f shows the designs of vertically oriented, large-radius (~20 mm) cylindrical flow chambers with three-dimensionally (3D) printed flat (Fig. 6a) and conical (Fig. 6f) end caps, in which we placed $N \approx 3{,}150$ or 9,500 spinners. The containers each have volumes of approximately 90 ml. When density matched (Fig. 6b,c,g,h) the spinners partition between a cloud in the vicinity of each end cap and a homogeneous bulk steady state of uniform density: a three-dimensional chiral fluid of active vortlets at intermediate Reynolds numbers.

The steady-state density of spinners is strongly influenced by the end-cap geometry. For flat end caps, the attractive interaction between spinners and a flat plate leads to the absorption of a carpet of spinners visible in the bottom of Fig. 6b,c. Once a sufficient density of spinners is absorbed, a dynamical equilibrium is reached in which spinners can re-suspend by sling-shotting each other into the bulk. In the case of conical end caps, the spinners roll along the surface as illustrated in the conical region in Fig. 6g and are ejected back into the bulk more efficiently, leading to a smaller number being sacrificed to the boundaries. The result of these differing offsets is clearly visible in Fig. 6b,c,g,h in which the same number of spinners are suspended in the same volume of fluid but the resulting density in the central region is dramatically different.

The different response to the boundary geometry is even more evident when gravity is used to compress the three-dimensional active chiral fluid against a boundary. For the flat plate (Fig. 6d), the result is a chiral fluid with varying density in the vertical direction and relatively

https://doi.org/10.1038/s41567-024-02651-5

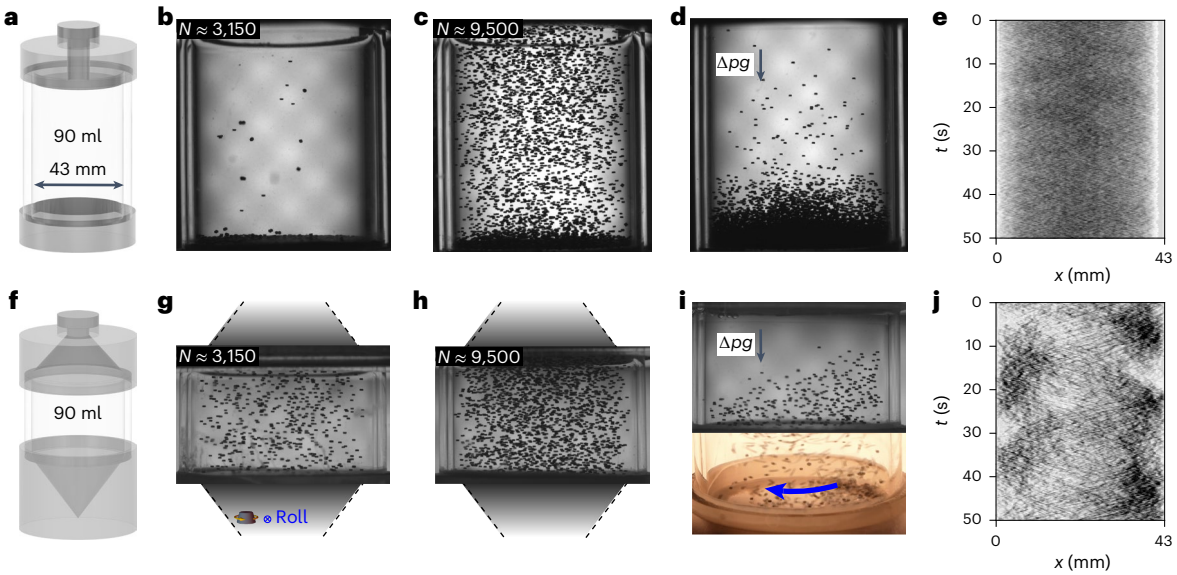


**Fig. 6 | Three-dimensional chiral active fluid in different geometries and under external force. a**, A diagram of a custom-made container consisting of flat 3D-printed top and bottom caps. **b**, With ~3,150 spinners at 30 Hz, most spinners are absorbed by the boundary. **c**, With ~9,500 spinners at 30 Hz, a dynamic steady state of a chiral active fluid emerges. **d**, By lowering the carrier fluid density, the chiral fluid is compressed down by gravity and exhibits a fluctuating surface. **e**, A vertically averaged kymograph of **d** shows no discernible dynamics. **f**, A diagram of a custom-made container consisting of conical 3D-printed top and bottom caps. **g**, With ~3,150 spinners at 30 Hz, more spinners are present in the bulk compared with **b**. The diagram at the bottom of the panel illustrates the rolling direction of a spinner pushed against a tilted surface. **h**, Approximately 9,500 spinners at 30 Hz in the conical cap cylinder shows a higher number density than that in **c**. From Supplementary Movie 6 we can observe there is a global rotation in the same direction of spin. **i**, With lower carrier fluid density, a twister state emerges where a group of spinners flocks along the edges. The arrow shows the direction of motion of the twister, which is opposite to the direction of spin. **j**, A vertically averaged kymograph showing the twister state in **i**. Panels **h** and **i** correspond to Supplementary Movie 6.

uniform distribution in the horizontal cross sections as verified by the vertically averaged kymograph in Fig. 6e. When the chiral fluid is instead compressed against a conical end cap (Fig. 6i), the result is a self-organized localized region of spinners (a twister) that orbits the flow chamber resulting in the spiralling kymograph shown in Fig. 6j. We note that the orbiting direction of the twister is opposite to the direction of spin, which we attribute to roll-like interactions between the spinners and the tilted boundary. This is in contrast to the density-matched case, in which a global rotational flow is established in the same direction of spin (Supplementary Movie 6). These experiments demonstrate that a three-dimensional chiral fluid can be built out of active vortlets. Both gravity and boundaries can be used to manipulate the fluid, and lively collective behaviour spontaneously and readily emerges.

The addition of inertia heralds a new regime for active matter in controlled settings, one in which the background flow plays an active role. Inertial flows are important for ordered formations of birds, where flock organization reflects the interaction of individuals with the vortical wakes of their neighbours[53]. However, it is difficult to separate the role of mechanics and sensing in living systems[54–56]. The synthetic system introduced here exhibits three-dimensional flocking due to hydrodynamic interactions, and this behaviour inherently relies on fluid inertia. Moreover, these nonlinear hydrodynamic interactions distinguish this system from classical active matter systems that exhibit flocking due to explicit alignment between neighbours[57].

The deceptively simple configuration we build upon—an axisymmetric particle rotating in an otherwise quiescent fluid—leverages flow inertia to give rise to novel hydrodynamic behaviours. A single spinner, which shares features with the two-sphere swimmer theorized in refs. 58,59, swims by mechanisms forbidden at low Reynolds numbers, yet differs substantially from both flapping swimmers, which rely on flow separation and vortex shedding[10,11], and oscillating swimmers in which a competition of inertial streaming flows and viscous drag leads to directed motion[12].

Collections of spinners with bound vortlets readily exhibit rich collective dynamics. Activated by internal rotations, these dynamics differ considerably from those of systems undergoing global rotation that are driven into two-dimensionality per the Taylor–Proudman theorem[60]. Finally, at high densities, spinner suspensions form a three-dimensional active chiral fluid, a new phase of matter in which particles generate and couple to nonlinear background flows.

## Online content

Any methods, additional references, Nature Portfolio reporting summaries, source data, extended data, supplementary information, acknowledgements, peer review information; details of author contributions and competing interests; and statements of data and code availability are available at https://doi.org/10.1038/s41567-024-02651-5.

## References

1. Shariff, K. & Leonard, A. Vortex rings. *Annu. Rev. Fluid Mech.* **24**, 235–279 (1992).
2. Saffman, P. G. in *Cambridge Monographs on Mechanics* 192–208 (Cambridge Univ. Press, 1993).
3. Needleman, D. & Dogic, Z. Active matter at the interface between materials science and cell biology. *Nat. Rev. Mater.* **2**, 17048 (2017).
4. Needleman, D. & Shelley, M. The stormy fluid dynamics of the living cell. *Phys. Today* **72**, 32–38 (2019).
5. Happel, J. & Brenner, H. Low Reynolds number hydrodynamics: with special applications to particulate media. In *Prentice-Hall International Series in the Physical and Chemical Engineering* 23–57 (Prentice-Hall, 1965).
6. Lauga, E. & Powers, T. R. The hydrodynamics of swimming microorganisms. *Rep. Progress Phys.* **72**, 096601 (2009).
7. Childress, S. & Dudley, R. Transition from ciliary to flapping mode in a swimming mollusc: flapping flight as a bifurcation in $Re_\omega$. *J. Fluid Mech.* **498**, 257–288 (2004).

8. Lauga, E. Continuous breakdown of Purcell's scallop theorem with inertia. *Phys. Fluids* **19**, 061703 (2007).
9. Klotsa, D. As above, so below, and also in between: mesoscale active matter in fluids. *Soft Matter* **15**, 8946–8950 (2019).
10. Vandenberghe, N., Zhang, J. & Childress, S. Symmetry breaking leads to forward flapping flight. *J. Fluid Mech.* **506**, 147–155 (2004).
11. Alben, S. & Shelley, M. Coherent locomotion as an attracting state for a free flapping body. *Proc. Natl Acad. Sci. USA* **102**, 11163–11166 (2005).
12. Klotsa, D., Baldwin, K. A., Hill, R. J., Bowley, R. & Swift, M. R. Propulsion of a two-sphere swimmer. *Phys. Rev. Lett.* **115**, 248102 (2015).
13. Klotsa, D., Swift, M. R., Bowley, R. M. & King, P. J. Chain formation of spheres in oscillatory fluid flows. *Phys. Rev. E* **79**, 021302 (2009).
14. Becker, A. D., Masoud, H., Newbolt, J. W., Shelley, M. & Ristroph, L. Hydrodynamic schooling of flapping swimmers. *Nat. Commun.* **6**, 8514 (2015).
15. Li, L. et al. Vortex phase matching as a strategy for schooling in robots and in fish. *Nat. Commun.* **11**, 5408 (2020).
16. Dombrowski, C., Cisneros, L., Chatkaew, S., Goldstein, R. E. & Kessler, J. O. Self-concentration and large-scale coherence in bacterial dynamics. *Phys. Rev. Lett.* **93**, 098103 (2004).
17. Sanchez, T., Chen, D. T. N., DeCamp, S. J., Heymann, M. & Dogic, Z. Spontaneous motion in hierarchically assembled active matter. *Nature* **491**, 431–434 (2012).
18. Palacci, J., Sacanna, S., Steinberg, A. P., Pine, D. J. & Chaikin, P. M. Living crystals of light-activated colloidal surfers. *Science* **339**, 936–940 (2013).
19. Bricard, A., Caussin, J.-B., Desreumaux, N., Dauchot, O. & Bartolo, D. Emergence of macroscopic directed motion in populations of motile colloids. *Nature* **503**, 95–98 (2013).
20. Wu, B., VanSaders, B., Lim, M. X. & Jaeger, H. M. Hydrodynamic coupling melts acoustically levitated crystalline rafts. *Proc. Natl Acad. Sci. USA* **120**, e2301625120 (2023).
21. Zhang, J., Alert, R., Yan, J., Wingreen, N. S. & Granick, S. Active phase separation by turning towards regions of higher density. *Nat. Phys.* **17**, 961–967 (2021).
22. Driscoll, M. et al. Unstable fronts and motile structures formed by microrollers. *Nat. Phys.* **13**, 375–379 (2017).
23. Kokot, G., Faizi, H. A., Pradillo, G. E., Snezhko, A. & Vlahovska, P. M. Spontaneous self-propulsion and nonequilibrium shape fluctuations of a droplet enclosing active particles. *Commun. Phys.* **5**, 91 (2022).
24. Mecke, J. & Ripoll, M. Birotor hydrodynamic microswimmers: from single to collective behaviour. *Europhys. Lett.* **142**, 27001 (2023).
25. Petroff, A. P., Wu, X.-L. & Libchaber, A. Fast-moving bacteria self-organize into active two-dimensional crystals of rotating cells. *Phys. Rev. Lett.* **114**, 158102 (2015).
26. Drescher, K. et al. Dancing volvox: hydrodynamic bound states of swimming algae. *Phys. Rev. Lett.* **102**, 168101 (2009).
27. Oppenheimer, N., Stein, D. B. & Shelley, M. J. Rotating membrane inclusions crystallize through hydrodynamic and steric interactions. *Phys. Rev. Lett.* **123**, 148101 (2019).
28. Tan, T. H. et al. Odd dynamics of living chiral crystals. *Nature* **607**, 287–293 (2022).
29. Wiegmann, P. & Abanov, A. G. Anomalous hydrodynamics of two-dimensional vortex fluids. *Phys. Rev. Lett.* **113**, 034501 (2014).
30. Hulsman, H. & Knaap, H. Experimental arrangements for measuring the five independent shear-viscosity coefficients in a polyatomic gas in a magnetic field. *Physica* **50**, 565–572 (1970).
31. Avron, J., Seiler, R. & Zograf, P. G. Viscosity of quantum hall fluids. *Phys. Rev. Lett.* **75**, 697 (1995).
32. Abanov, A. G., Can, T. & Ganeshan, S. Odd surface waves in two-dimensional incompressible fluids. *SciPost Phys.* **5**, 010 (2018).
33. Knaap, H. & Beenakker, J. Heat conductivity and viscosity of a gas of non-spherical molecules in a magnetic field. *Physica* **33**, 643–670 (1967).
34. Banerjee, D., Souslov, A., Abanov, A. G. & Vitelli, V. Odd viscosity in chiral active fluids. *Nat. Commun.* **8**, 1573 (2017).
35. Soni, V. et al. The odd free surface flows of a colloidal chiral fluid. *Nat. Phys.* **15**, 1188–1194 (2019).
36. Bililign, E. S. et al. Motile dislocations knead odd crystals into whorls. *Nat. Phys.* **18**, 212–218 (2022).
37. Banerjee, D., Souslov, A. & Vitelli, V. Hydrodynamic correlation functions of chiral active fluids. *Phys. Rev. Fluids* **7**, 043301 (2022).
38. Bowick, M. J., Fakhri, N., Marchetti, M. C. & Ramaswamy, S. Symmetry, thermodynamics, and topology in active matter. *Phys. Rev. X* **12**, 010501 (2022).
39. Mecke, J. et al. Simultaneous emergence of active turbulence and odd viscosity in a colloidal chiral active system. *Commun. Phys.* **6**, 1–13 (2023).
40. Guazzelli, E., Morris, J. F. & Pic, S. in *Cambridge Texts in Applied Mathematics* 192–212 (Cambridge Univ. Press, 2011).
41. Grzybowski, B. A., Stone, H. A. & Whitesides, G. M. Dynamic self-assembly of magnetized, millimetre-sized objects rotating at a liquid–air interface. *Nature* **405**, 1033–1036 (2000).
42. Bickley, W. The secondary flow due to a sphere rotating in a viscous fluid. *Lond. Edinb. Dubl. Philos. Mag. J. Sci.* **25**, 746–752 (1938).
43. Climent, E., Yeo, K., Maxey, M. R. & Karniadakis, G. E. Dynamic self-assembly of spinning particles. *J. Fluids Eng.* **129**, 379–387 (2006).
44. Ovseenko, R. I. & Ovseenko, Y. G. Drag of a rotating sphere. *Fluid Dyn.* **3**, 78–82 (1968).
45. Schlichting, H. & Gersten, K. *Boundary Layer Theory* (Springer, 2017).
46. Angot, P., Bruneau, C.-H. & Fabrie, P. A penalization method to take into account obstacles in incompressible viscous flows. *Num. Math.* **81**, 497–520 (1999).
47. Hester, E. W., Vasil, G. M. & Burns, K. J. Improving accuracy of volume penalised fluid–solid interactions. *J. Comput. Phys.* **430**, 110043 (2021).
48. Hayday, A. A. Similar flows about axisymmetric bodies rotating in a fluid at rest. *Appl. Sci. Res. Sect. A* **14**, 405–419 (1965).
49. Halsey, T. C., Anderson, R. A. & Martin, J. E. The rotary electrorheological effect. *Int. J. Mod. Phys. B* **10**, 3019–3027 (1996).
50. Klapp, S. H. Collective dynamics of dipolar and multipolar colloids: from passive to active systems. *Curr. Opin. Colloid Interf. Sci.* **21**, 76–85 (2016).
51. Partridge, B. L., Pitcher, T., Cullen, J. M. & Wilson, J. The three-dimensional structure of fish schools. *Behav. Ecol. Sociobiol.* **6**, 277–288 (1980).
52. Liu, Q. & Prosperetti, A. Wall effects on a rotating sphere. *J. Fluid Mech.* **657**, 1–21 (2010).
53. Portugal, S. J. et al. Upwash exploitation and downwash avoidance by flap phasing in ibis formation flight. *Nature* **505**, 399–402 (2014).
54. Attanasi, A. et al. Collective behaviour without collective order in wild swarms of midges. *PLoS Comput. Biol.* **10**, 1–10 (2014).
55. Cavagna, A. & Giardina, I. Bird flocks as condensed matter. *Annu. Rev. Condens. Matter Phys.* **5**, 183–207 (2014).
56. Bain, N. & Bartolo, D. Dynamic response and hydrodynamics of polarized crowds. *Science* **363**, 46–49 (2019).
57. Vicsek, T., Czirók, A., Ben-Jacob, E., Cohen, I. & Shochet, O. Novel type of phase transition in a system of self-driven particles. *Phys. Rev. Lett.* **75**, 1226–1229 (1995).

58. Nadal, F., Pak, O. S., Zhu, L., Brandt, L. & Lauga, E. Rotational propulsion enabled by inertia. *Eur. Phys. J. E* **37**, 60 (2014).
59. Cox, R. G. The steady motion of a particle of arbitrary shape at small Reynolds numbers. *J. Fluid Mech.* **23**, 625–643 (1965).
60. Pedlosky, J. *Geophysical Fluid Dynamics* (Springer, 2013).

## Data availability

The data contained in the plots within this paper and other findings of this study are available from the corresponding author on reasonable request.

## Code availability

Codes used to analyse data are available from the corresponding author upon reasonable request.

## Acknowledgements

We thank P. Vlahovska for scientific discussions, S. Ray for early development of the experimental platform and L. Mazzenga for his guidance in particle fabrication. This work was primarily supported by NSF DMR-2011854. Additional support was provided by NSF DMR-1905974, and the Brown Foundation. S.A. acknowledges support from NSF DMR-1905974 and a Grainger Fellowship at the University of Chicago. This work pertains to "Investissements d'Avenir" (LABEX INTERACTIFS, reference ANR-11-LABX-0017-01, and EUR INTREE, reference ANR-18-EURE-0010). This work made use of the shared facilities at the University of Chicago Materials Research Science and Engineering Center, supported by the National Science Foundation under award number DMR-2011854. The computations in this work were performed at facilities supported by the Scientific Computing Core at the Flatiron Institute, a division of the Simons Foundation.

## Author contributions

W.T.M.I. and M.J.S. conceived and supervised research. S.A. and W.T.M.I. designed early experiments and S.A. performed early experiments that included the observation of flock formation. P.C. and S.A. developed and performed further, more refined, experiments. S.W. formulated analytical and numerical models, and performed simulations. S.W. and P.C. integrated experimental, numerical and theoretical results including self-propulsion and collective dynamics. T.M., P.C., S.A. and S.W. performed PIV measurements. All authors analysed data and prepared the manuscript.

## Competing interests

The authors declare that they have no competing interests.

## Additional information

**Supplementary information** The online version contains supplementary material available at https://doi.org/10.1038/s41567-024-02651-5.

**Correspondence and requests for materials** should be addressed to Michael J. Shelley or William T. M. Irvine.

**Peer review information** *Nature Physics* thanks the anonymous reviewers for their contribution to the peer review of this work.